



## Effects of capillarity on pool boiling using nano-textured surfaces through electro sprayed $\text{BiVO}_4$ nano-pillars



Hong Seok Jo<sup>a,1</sup>, Min-Woo Kim<sup>a,1</sup>, Karam Kim<sup>a</sup>, Seongpil An<sup>a</sup>, Yong Il Kim<sup>a</sup>, Scott C. James<sup>b</sup>, Jeehoon Choi<sup>c,\*</sup>, Sam S. Yoon<sup>a,\*</sup>

<sup>a</sup> School of Mechanical Engineering, Korea University, Seoul 02841, Republic of Korea

<sup>b</sup> Depts. of Geosciences and Mechanical Engineering, Baylor University, Waco, TX 76798, USA

<sup>c</sup> LG Electronics Inc., Seoul, Republic of Korea

### HIGHLIGHTS

- Pool boiling enhancement through wettability control using nanotextured surfaces was demonstrated.
- Bismuth vanadate ( $\text{BiVO}_4$ ) was electro sprayed and nano-pillars are formed.
- The nano-pillars provided numerous bubble nucleation sites because of increased surface area.
- Both the critical heat flux and effective heat transfer coefficient increased with nano-pillar height.

### ARTICLE INFO

#### Article history:

Received 15 January 2017

Received in revised form 10 May 2017

Accepted 15 May 2017

Available online 17 May 2017

#### Keywords:

Electrospraying

Bismuth vanadate

Pool boiling

Superheat temperature

Critical heat flux

### ABSTRACT

Pool boiling is a mechanism by which heat is removed by changing the phase of a coolant from liquid to vapor. Surface wettability, which drives coolant capillarity, has a profound effect on the boiling process. We demonstrate pool boiling enhancement through wettability control using electro sprayed, nano-textured surfaces of bismuth vanadate ( $\text{BiVO}_4$ ). When a  $\text{BiVO}_4$  liquid precursor is electrostatically charged and sprayed, submicron droplets are formed and their acceleration is driven by the electrostatic force established between the nozzle exit and substrate. As droplets approach the substrate, Brownian diffusion takes place and an opposing thermophoretic force impedes the dynamic motion of evaporating droplets. As a result, nano-pillars are formed, whose physical sizes change the wettability of a surface and change pool-boiling phenomenon. The surface wettabilities of nano-textured surfaces were quantified with the water contact angle. Increased spraying time resulted in greater nano-pillar structure heights. Both the critical heat flux and effective heat transfer coefficient increased with nano-pillar height. However, excessively tall pillars had an adverse effect on pool-boiling through trapping of nucleated bubbles near the heat surface, which hindered efficient heat transfer.

© 2017 Published by Elsevier Ltd.

### 1. Introduction

The efficiency and performance of electronics devices depend upon passively or actively dissipating high heat loads while maintaining low operating temperatures. To achieve a satisfactory thermal management solution, a number of cooling technologies have been introduced including active cooling combined with liquid-vapor phase-change heat-transfer technologies, i.e. heat pipes, thermosiphons, and vapor chambers (Agostini et al., 2007; Leong et al., 2017; Weibel et al., 2010). These techniques dissipate a large

amount of heat under constraints such as confined spaces, maximum allowable operating temperatures, and low noise (Bar-Cohen et al., 2006; Choi et al., 2012; Marcinichen et al., 2013; Semenic et al., 2008; Shabgard et al., 2015). Nevertheless, thermal management remains of significant interest due to increased-functionality, size-reduction, and lightweight-platform requirements (Choi and Jeong, 2016). One way to deal with these challenges is to improve the heat transfer rate of conventional active-cooling solutions and employ nano-texturing to enhance phase-change heat-transfer performance.

In our previous studies, advanced nano-textured surfaces were designed with varying wettability, texturing time (texture thickness), and texture structure (Jo et al., 2017). Hydrophilic nano-textured surfaces increased critical heat flux (CHF) through an increased number of nucleation sites. Nanoscale cavities

\* Corresponding author.

E-mail addresses: [choijeehoon@gmail.com](mailto:choijeehoon@gmail.com) (J. Choi), [skymoon@korea.ac.kr](mailto:skymoon@korea.ac.kr) (S.S. Yoon).

<sup>1</sup> These authors have equally contributed.

generate bubbles within the surface, but high capillary-assisted liquid flow is needed because vapor pockets block liquid intrusion.

In this effort, a new approach is explored to balance high capillary pressure and high permeability in nano-textured surfaces. Bismuth vanadate ( $\text{BiVO}_4$ ) nano-pillars increase the number of nucleation sites due to increased surface area, which also connects liquid-vapor escape paths and enhances capillary-assisted liquid flow. Numerous cavities are available in  $\text{BiVO}_4$  nano-pillar surfaces, which offer abundant bubble nucleation sites that enhance pool-boiling heat transfer. In addition, the nano-pillar structure imposes alternating regions of high capillary-assisted liquid flow and low resistance to vapor flow through separation of the liquid and vapor phases. Fabrication and testing of these nano-pillar structures and their effects on pool boiling heat transfer are described.

Bismuth vanadate nano-textured surfaces are characterized by scanning electron microscopy (SEM), atomic force microscopy (AFM), and X-ray photoelectron spectroscopy (XPS). The diffusion aggregation phenomenon by which the nano-pillars are formed is briefly explained. Various electro-spraying times produced films of various wettability, which was measured qualitatively by observing the capillary action of a fluid on a textured surface. CHF and the onset of boiling (ONB) were experimentally measured. Effective heat transfer coefficients ( $h_{\text{eff}}$ ) for variously textured surfaces were quantified. A phenomenological description of the pool-boiling process with respect to the  $\text{BiVO}_4$ -textured surface is also provided through snapshots of bubble nucleation and departure captured with a high-speed CCD camera.

## 2. Experimental setup

### 2.1. Materials

$\text{BiVO}_4$  was selected for study because it yields a unique nano-pillared surface through a diffusion-limited aggregation process (Yoon et al., 2015). The  $\text{BiVO}_4$  precursor was prepared by dissolving 1.08 g of bismuth (III) nitrate pentahydrate ( $\text{BiN}_3\text{O}_9 \cdot 5\text{H}_2\text{O}$ ,  $\geq 98\%$ , Sigma-Aldrich) and 0.78 g of vanadium (III) acetylacetonate ( $\text{C}_{15}\text{H}_{21}\text{O}_6\text{V}$ , 97%, Sigma-Aldrich) into 10 ml of acetic acid ( $\text{CH}_3\text{COOH}$ , 99.7%, Samchun Chemicals). This solution was magnetically stirred at room temperature. The stoichiometry of Bi and V in the  $\text{BiVO}_4$  precursor was 1:1. The thermal conductivity of  $\text{BiVO}_4$  is expected to fall between the  $5.8 \text{ W m}^{-1} \text{ K}^{-1}$  of bismuth vanadate and the  $7.97 \text{ W m}^{-1} \text{ K}^{-1}$  of vanadium oxide.

### 2.2. Electro-spraying

Prior to  $\text{BiVO}_4$  electrostatic spray deposition (ESD), the substrates were cleaned in an ultrasonic bath and dried. The 3-mm ID nozzle was orthogonally aligned with the plate and the nozzle-to-substrate distance was 45 mm with a  $40^\circ$  cone angle. The area of the indium tin oxide (ITO)-coated glass was  $25 \times 25 \text{ mm}^2$  and the diameter of the copper substrate was 20 mm. The  $\text{BiVO}_4$  precursor was supplied to the nozzle through a syringe pump (Legato 100, KDS) and a stable cone jet generated fine droplets. A high-DC voltage was applied to the tip of a nozzle by a DC power supply (EL20P2, Glassman high voltage). The  $\text{BiVO}_4$  layer was deposited on the substrate, which was maintained at  $80^\circ\text{C}$ . The nano-pillared surface is always so thin that it is unlikely that significant additional thermal resistance is inherited from even the thickest of nano-layers studied here.

### 2.3. Pool boiling

Pool boiling in when liquid evaporates at a solid-liquid interface when the surface temperature ( $T_s$ ) exceeds the saturation

temperature ( $T_{\text{sat}}$ ) of the liquid. Heat transfer from the solid surface to the liquid is calculated from Newton's Law of Cooling as:

$$q'' = h_{\text{eff}}(T_s - T_{\text{sat}}) = h_{\text{eff}}\Delta T_{\text{sat}}, \quad (1)$$

where  $q''$  and  $\Delta T_{\text{sat}}$  are the heat flux and superheat. In general, pool-boiling phenomena are classified by dividing  $\Delta T_{\text{sat}}$  into four regimes, namely natural convection, nucleate boiling, transition boiling, and film boiling. Superheat,  $\Delta T_{\text{sat}} = T_s - T_{\text{sat}}$ , is estimated as:

$$\Delta T_{\text{sat}} = T_1 - \frac{k_{\text{Al}}(T_2 - T_1)\Delta x_w}{k_{\text{Cu}}\Delta x_{12}} - T_f, \quad (2)$$

where  $k_{\text{Cu}}$  ( $401 \text{ W m}^{-1} \text{ K}^{-1}$ ),  $k_{\text{Al}}$  ( $210 \text{ W m}^{-1} \text{ K}^{-1}$ ), and  $\Delta x_w$  are the thermal conductivities of the copper substrate and the aluminum rod and the distance between thermocouple  $T_1$  and the substrate surface, respectively.  $\Delta T_{\text{sat}}$  can be calculated from Eq. (2) assuming equal heat flux in the aluminum rod and the copper substrate and  $T_{\text{sat}} = T_f$ .

The heat flux to water from the substrate surface is assumed one-dimensional and calculated from Fourier's Law as:

$$q'' = k_{\text{Al}} \frac{T_1 - T_2}{\Delta x_{12}} = k_{\text{Al}} \frac{T_2 - T_3}{\Delta x_{23}}, \quad (3)$$

where  $\Delta x_{12}$  and  $\Delta x_{23}$  are equal to the 8 mm between thermocouples. When using Eqs. (2) and (3),  $h_{\text{eff}} = q''/\Delta T_{\text{sat}}$  was estimated from Eq. (1).

Fig. 1 is a schematic of the experimental setup comprising a glass chamber, a condensing unit, two DC power supplies, a data-recording unit, and ceramic heaters to transfer heat to the copper substrates. The copper substrate coated with  $\text{BiVO}_4$  was placed on the main aluminum rod and the three preheaters inside the glass chamber were supplied with 80 V to maintain the water temperature at  $100^\circ\text{C}$ . The four ceramic heaters applied 30 V for about 30 min and the copper substrate temperature reached almost  $100^\circ\text{C}$ . When the copper substrate and the water were almost at the saturation temperature, the power supply connected to the four ceramic heaters increased voltage from 30 to 120 V. K-type thermocouples (Omega) with thicknesses of 1 mm and accuracies of  $\pm 0.3^\circ\text{C}$  were connected to a data recorder (LR8400-200, HIOKI) and the temperature was measured. To ensure data quality, at least five experimental replicates were completed for each characterization and the average of these is presented.

The experimental uncertainty in heat flux was estimated using an error propagation method as (Holman, 2001):

$$U_q = \sqrt{\left(\frac{\partial q}{\partial V} U_V\right)^2 + \left(\frac{\partial q}{\partial I} U_I\right)^2 + \left(\frac{\partial q}{\partial A} U_A\right)^2}. \quad (4)$$

Uncertainty from the preceding equation is  $\pm 4.3\%$  for  $q''$ .

### 2.4. Characterization

The morphology of the  $\text{BiVO}_4$  layer was measured using a field-emission scanning electron microscope (FE-SEM, S-5000, Hitachi) at 15 kV and the roughness of each 3D image was characterized by an optical profiler (OP, Veeco, NT-1100). The chemical composition and bond were analyzed with X-ray photoelectron spectroscopy (XPS, X-TOOL, ULVAC-PHI) and crystallinity was measured using X-ray diffraction (XRD, Smart Lab, Rigaku, Al K radiation over a  $2\theta$  range of  $20\text{--}80^\circ$ ). Capillary phenomena were measured by applying water droplets to the sample and measuring water contact angles by taking snapshots with a high-speed camera (Phantom 9.1, Vision research Inc.).

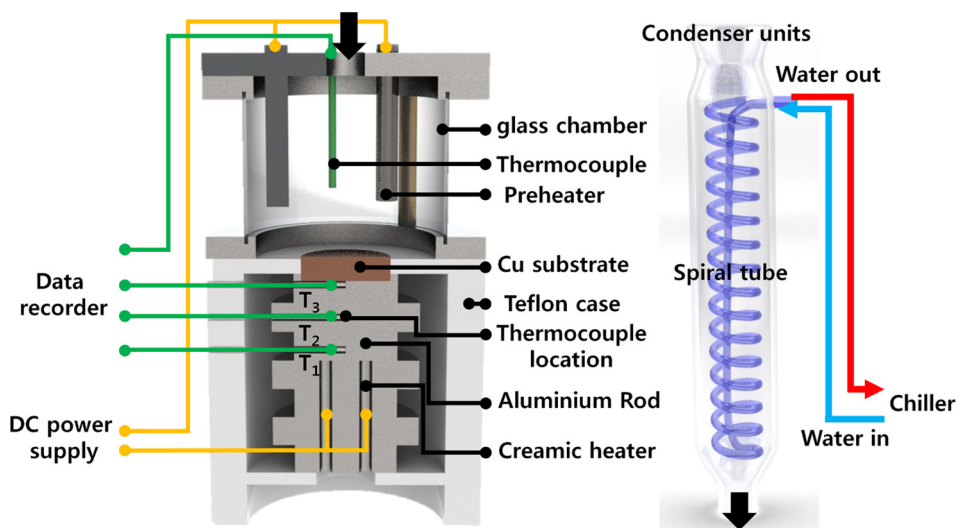


Fig. 1. Schematics of the plate pool-boiling facility; a cross-section view of the experimental pool-boiling setup and the condenser unit installed on the top of the pool-boiling setup.

### 3. Results and discussion

#### 3.1. Pillar-like structure of the $\text{BiVO}_4$

This study varied ESD times ( $t_e$ ) in contrast to previous studies (Yoon et al., 2015). The lengths of the  $\text{BiVO}_4$  pillars increased from approximately 0.8 to 12  $\mu\text{m}$  when  $t_e$  increased from 10 to 80 min. To study the effects of the pillar length, ESD was conducted for 0.5, 1, and 2 h. The various surface morphologies of the  $\text{BiVO}_4$  layers (top and cross-sectional views) are shown in Fig. 2a–c for the varied  $t_e$ .  $\text{BiVO}_4$  was deposited as a fractal-like structure (top view) and the pillar structure is clearly observed in the second row of Fig. 2.  $\text{BiVO}_4$  began to develop the nano-textured pillar-like structure when  $t_e = 0.5$  h. Upon increasing  $t_e$  from 0.5 to 2 h, pillar length grew as listed in Table 1 and the pillars formed colonies. With increasing pillar length, surface roughness also increased dramatically as shown in Fig. 2d and Table 1.

As shown in Fig. 3a of the XRD pattern, the diffraction peaks of  $\text{BiVO}_4$  annealed at 500  $^\circ\text{C}$  matched the monoclinic structure of  $\text{BiVO}_4$  in the literature (JCPDS No. 83-1700). The diffraction peaks correspond to the 110, 121, 040, 200, 002, 141, 211, 112, 150, 051, 132, 240, 042, 202, 161, 251, 152, 321, and 123 planes, respectively.

To investigate the surface compositions of the  $\text{BiVO}_4$ , XPS was undertaken. As shown in the XPS spectrum (Fig. 3b), Bi and V elements were detected. The peaks with binding energies in the high-resolution XPS spectrum of Bi 4f were 158.5 and 163.7 eV correspond to Bi 4f<sub>7/2</sub> and Bi 4f<sub>5/2</sub>, respectively (Fig. 3c) (Ju et al., 2016). Moreover, the binding energies of Bi 4f<sub>7/2</sub> were deconvoluted into two peaks at 158 and 159 eV. In addition, Bi 4f<sub>5/2</sub> could be also deconvoluted into two peaks at around 163.5 and 164.5 eV. The binding energies of V 2p split into different two peaks at approximately 516.3 and 523.5 eV correspond to the V 2p<sub>1/2</sub> and V 2p<sub>3/2</sub> orbitals, respectively (Zhang et al., 2013). Moreover, the binding energies of V 2p<sub>1/2</sub> and V 2p<sub>3/2</sub> could be divided into two peaks (Fig. 3d).

#### 3.2. Mechanism of pillar structure

The formation of a pillar-like  $\text{BiVO}_4$  layer deposited by electrostatic spray has been previously described as an analytical function of droplet motion affected by the surrounding air flow, thermal

diffusion, thermophoresis, and electrophoresis (Yoon et al., 2015). In addition, the morphology of the deposited layer was described through various dimensionless parameters.

Fig. 4 is a schematic of the formation of a pillar-like  $\text{BiVO}_4$  layer. The state of  $\text{BiVO}_4$  droplets depends upon the regime. First, droplets issue from the nozzle as a liquid. Second, accelerated by air, droplets evaporate into a semi-liquid state. Finally, when the semi-liquid droplets arrive at the substrate surface, the remaining solvent is evaporated on the heated substrate to leave  $\text{BiVO}_4$  particles.

The dynamics of the electrically charged droplets are strongly influenced by the electric field. As droplets attach onto the surface, roughness increases, which initiates pillar formation. This roughness concentrates the electric field, further promoting particle attachment that grow into pillars. As pillars grow, a strong gradient in the electric field is formed at the pillar tip because the distance to the nozzle tip is shorter and pillar growth is reinforced. If the potential at a distance  $r$  from a sphere carrying charge  $Q$  is (Halliday, 1991):

$$V = \frac{1}{4\pi\epsilon_0} \frac{Q}{r}, \quad (5)$$

where  $\epsilon_0$  is the permittivity, then the charge density on the sphere surface is

$$\sigma = \frac{Q}{4\pi r^2} = \frac{V\epsilon_0}{r}, \quad (6)$$

which is inversely proportional  $r$ .

In the center schematic of Fig. 4,  $\text{BiVO}_4$  particles form the rough surface composed of a large number of small spheres. The electric field at  $\text{BiVO}_4$  particles is stronger than that near an uncoated surface. So, incoming  $\text{BiVO}_4$  particles are attracted to deposited  $\text{BiVO}_4$  particles, which further increases electric field strength as deposited particles form pillars.

#### 3.3. Effect of roughness on capillary rise and water angle

Water contact angle (WCA) characterizes surface wettability, which is related to the surface energy of sessile drops on a substrate (Eick et al., 1975; Kwok et al., 1995). However, this method has certain limitations because WCA can change with drop size. To avoid such complications, the method uses capillary rise on a nearly vertical plate to determine WCA.

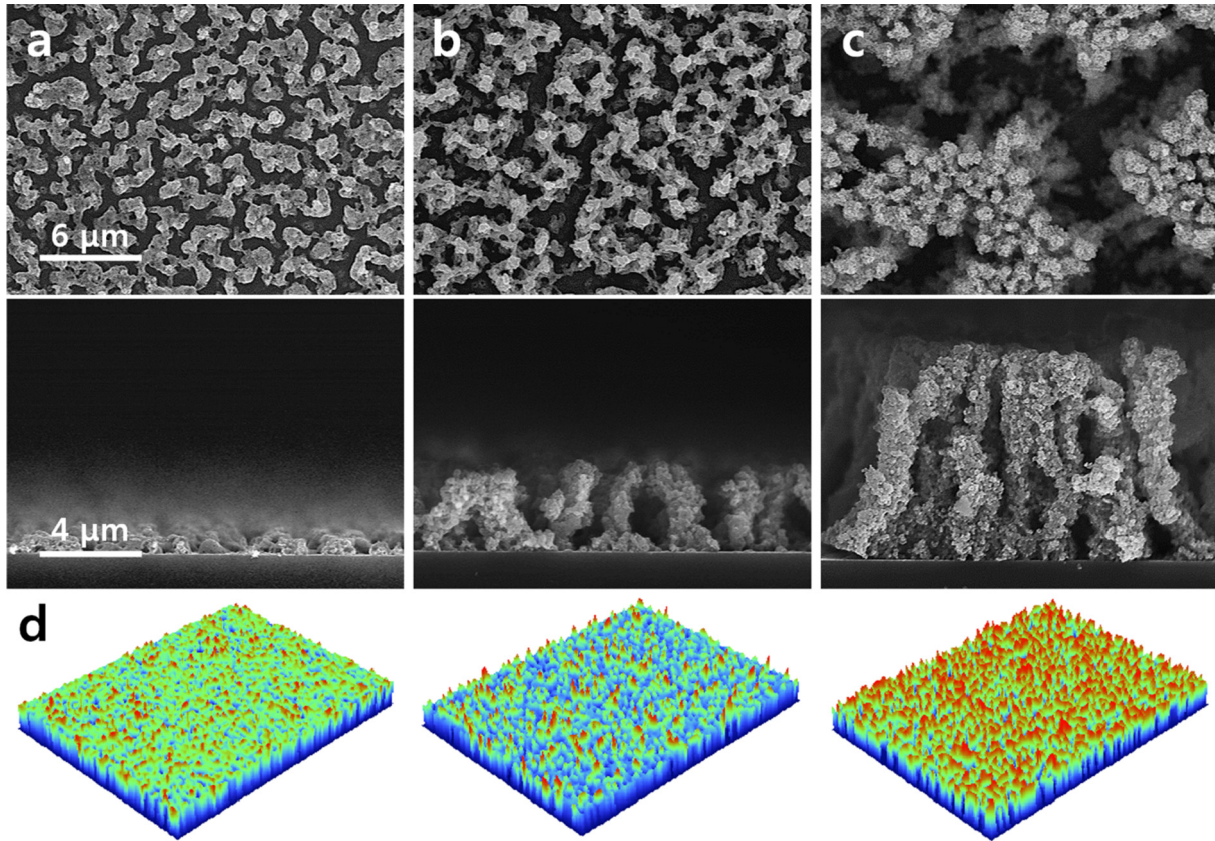


Fig. 2. (a)–(c) SEM images of the BiVO<sub>4</sub> pillars for increasing  $t_e$  (top and side) and (d) OP images of each case.

Table 1

Roughness of the BiVO<sub>4</sub> pillars subject to increasing  $t_e$ .

$t_e$ [h]	Length [ $\mu\text{m}$ ]	Roughness [nm]
0.5	0.725	72.5
1	4.24	267.2
2	8.76	3090

The ITO glass coated with BiVO<sub>4</sub> was dipped in water vertically and water rises against gravity by according to the capillary. The capillary rise is obtained from the Laplace equation for a cylindrical liquid surface as (Eick et al., 1975):

$$-\frac{d \cos \Phi}{dz} = \frac{\Delta \rho g z}{\gamma_{LV}} = Cz \quad (7)$$

where  $C = \Delta \rho g z / \gamma_{LV}$ , and  $\Delta \rho$  is the density difference between liquid and vapor (998 kg/m<sup>3</sup>),  $g$  is gravitational acceleration, and  $\gamma_{LV} = 0.72$  nM/m is the liquid surface tension. Variables  $z$  and  $\Phi$  are illustrated in Fig. 5a. Integrating the preceding equation and assuming  $z = h$  and  $\Phi = 90 - (\theta + \beta)$  yields:

$$h^2 = \frac{2\gamma_{LV}}{\Delta \rho g} [1 - \sin(\theta + \beta)]. \quad (8)$$

This equation estimates WCA ( $\theta$ ) and the theoretical  $h$  favorably compared to the measured  $h$  through snapshots. When measuring capillary rise, the ITO glass with BiVO<sub>4</sub> was tilted by  $\beta = 3^\circ$  from vertical. In Table 2, WCA decreased with increasing  $t_e$  while  $h$  calculated from Eq. (4) also increased. Measured  $h$  was almost equal with the theoretical  $h$  at  $t_e = 0.5$  and 1 h although deviation was observed at  $t_e = 2$  h. This observation confirms that capillary rise increases with surface roughness as shown in Fig. 5b.

### 3.4. Effect of the nanotextured layer on pool boiling

The pool-boiling experiments were conducted at atmospheric pressure with distilled water. Experimental results are plotted in Fig. 6 and presented in terms of  $q''$ ,  $\Delta T_{\text{sat}}$ , CHF, and  $h_{\text{eff}}$ . All data were obtained at a given heat flux under steady-state conditions. BiVO<sub>4</sub>-textured substrates were compared to an uncoated substrate. Fig. 6a presents  $q''$  as a function of  $\Delta T_{\text{sat}}$  while Fig. 6b shows how  $h_{\text{eff}}$  varies with  $q''$ . CHF and  $h_{\text{eff}}$  for an uncoated substrate were 66.3 and 1.26 kW m<sup>-2</sup> k<sup>-1</sup>, respectively. The boiling results for the uncoated substrate are consistent with other experimental result (An et al., 2016). Clearly, increased nucleation-site density due to BiVO<sub>4</sub> texturing resulted in substantially better heat-transfer performance. Moreover, the  $\Delta T_{\text{sat}}$  of all BiVO<sub>4</sub> coatings were significantly reduced thereby increasing  $h_{\text{eff}}$ . The CHF and  $h_{\text{eff}}$  for  $t_e = 0.5, 1$  and 2 h are 85.2, 102.2, and 97.5 kW m<sup>-2</sup>, respectively, and 1.6, 2.4, and 2.2 kW m<sup>-2</sup> k<sup>-1</sup>, respectively. The fact that CHFs are independent of  $t_e$  suggests they are not a strong function of nucleation-site density. Further understanding of these phenomena can be gleaned from Fig. 7, which is a schematic of bubble departure. For an uncoated substrate, bubble incipience occurs at  $\Delta T_{\text{sat}} = 25^\circ\text{C}$  as denoted by the ONB evident in Fig. 6a after natural convection. The ONB for all BiVO<sub>4</sub> coatings occurred earlier. A possible explanation for this finding is that embryonic bubble radii associated with the nano-pores of the BiVO<sub>4</sub> pillars facilitate an increase in bubble-departure frequency, which could reduce superheat. In addition, as depicted in Fig. 7b, an increase in surface area of the BiVO<sub>4</sub> pillars (provided with sufficient supply of liquid by capillary forces) enhanced the CHF. Although two phases coexist in the BiVO<sub>4</sub> pillars, the small, frequently formed bubbles can escape through the narrow spaces between the BiVO<sub>4</sub> pillars. For  $t_e > 1$  h, however, the narrow spaces between tall BiVO<sub>4</sub> pillars

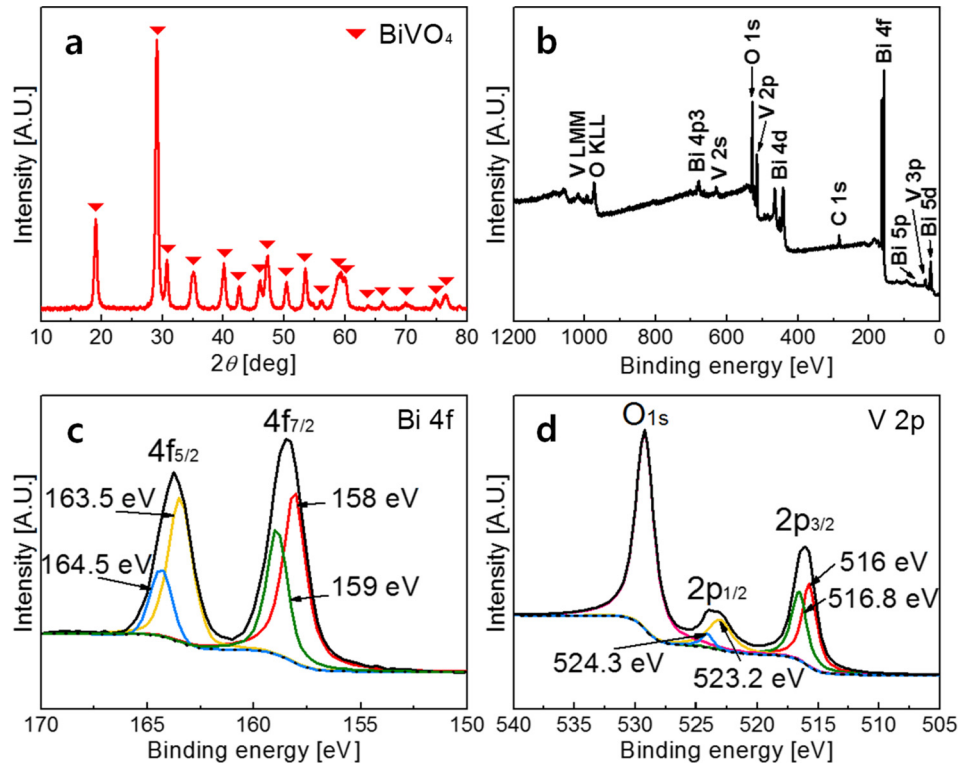


Fig. 3. (a) XRD pattern of the  $\text{BiVO}_4$  annealed at  $500^\circ\text{C}$  and XPS spectra of (b) survey spectrum, (c) Bi 4f, and (d) V 2p.

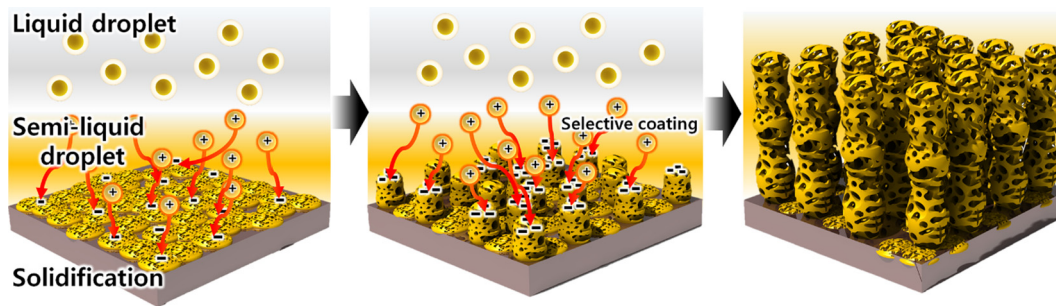


Fig. 4. Schematic of the  $\text{BiVO}_4$  coating mechanism.

(see Fig. 1) impede the migration of the bubbles, which most likely form toward the middle and bottom of the  $\text{BiVO}_4$  pillars. Bubbles generated near the top of the  $\text{BiVO}_4$  pillars also impede the flow of liquid to the wall, which, in turn, allows a rapid increase in wall temperature. Therefore, the CHF and superheat of the  $\text{BiVO}_4$  pillars for  $t_e = 2$  h are lower than that for  $\text{BiVO}_4$  pillars with  $t_e < 1$  h. Thus, it appears that the height of the  $\text{BiVO}_4$  pillars should be limited despite the improved liquid supply resulting from the increased capillary forces.

Fig. 8 shows pool-boiling photographs taken at 3,400 frames per second under 250-W halogen lighting. Once again, the photographs confirm numerous bubbles generated more frequently in  $\text{BiVO}_4$  pillars compared to an uncoated substrate at the ONB, the highest  $h_{\text{eff}}$ , and the CHF.

In Fig. 7b, pillars draw in water near the bottom through capillary forces and bubbles form on the nano-textured pillar surfaces. For  $t_e = 1$  h, the ONB occurred at lowest  $\Delta T_{\text{sat}}$ , which has the lowest  $T_s$ . Rapid formation of bubbles facilitates cooling, which decreases  $T_s$ .

At the base of the  $\text{BiVO}_4$  layer, pillars draw in water through enhanced capillary forces. Near the top of the  $\text{BiVO}_4$  layer, bubbles

are formed and released from the nucleation sites, facilitating the ONB. These capillary force and the mechanism of bubble formation depend upon the surface morphology as shown in Fig. 1a–c. The pillar-like  $\text{BiVO}_4$  coating in Fig. 1b facilitates bubble formation and release due to appropriate length of and distance between pillars. However, when  $t_e$  is excessive, the space between nano-pillars diminishes. As a result, nucleated bubbles are less easily released because of the tortuous pathways they must follow to escape from between the pillars, which hinders efficient cooling. In other words, an optimal  $t_e$  is sought to yield the best possible cooling scenario that efficiently promotes both capillary forces and bubble formation and release.

Although bubbles are eventually released, their delay inhibits cooling resulting in higher  $T_s$ . Because of this phenomenon, the slopes of the curves in Fig. 6b differ. These slopes, the ratio between  $q''$  and  $\Delta T_{\text{sat}}$  quantify the  $h_{\text{eff}}$  due to texturing with  $\text{BiVO}_4$  pillars. Because the largest  $h_{\text{eff}}$  is for  $t_e = 1$  h, the corresponding pillar length and distance between pillars is more suitable than others for removing heat.

Transition boiling starts at the CHF and leads to the maximum  $q''$  shown in Fig. 6, similarly for  $h_{\text{eff}}$ . The CHF increases because

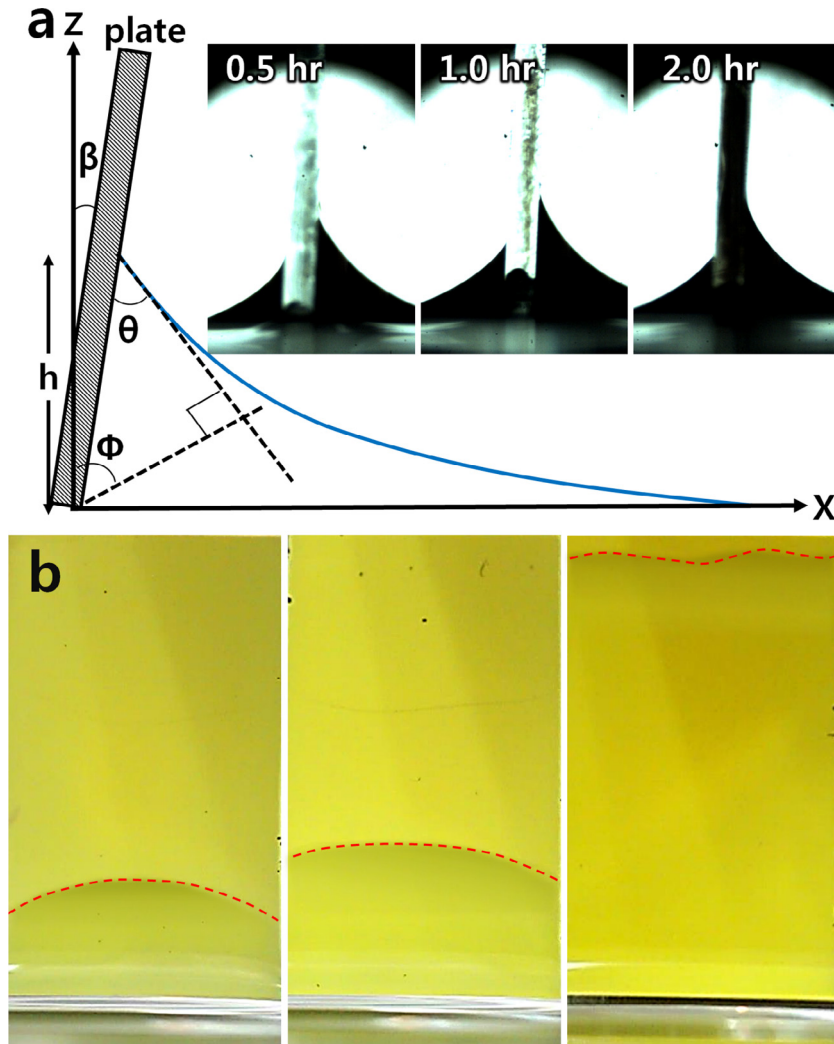


Fig. 5. (a) Schematic of capillary rise at a angled wall and (b) the corresponding photographs of capillary phenomena for  $t_e$  from 0.5 to 2 h.

**Table 2**  
WCA and the theoretical and measured capillary rises on the BiVO<sub>4</sub> layer for increasing  $t_e$ .

$t_e$ [h]	WCA [°]	Theoretical $h$ [mm]	Measured $h$ [mm]
0.5	16	3.15	3.23
1	8.9	3.42	3.55
2	1.5	3.70	4.01

more nucleation sites produce more bubbles to remove heat. In Fig. 6a, CHF is lowest for the uncoated substrate. BiVO<sub>4</sub> texturing increases CHF as in photographs Fig. 8a and b of the boiling regimes: natural convection, ONB, maximum  $h_{eff}$ , CFH, and transition boiling. Because texturing increases the water-contact surface area, nucleation sites and the number of released bubbles commensurately increase. Moreover, bubble sizes are smaller

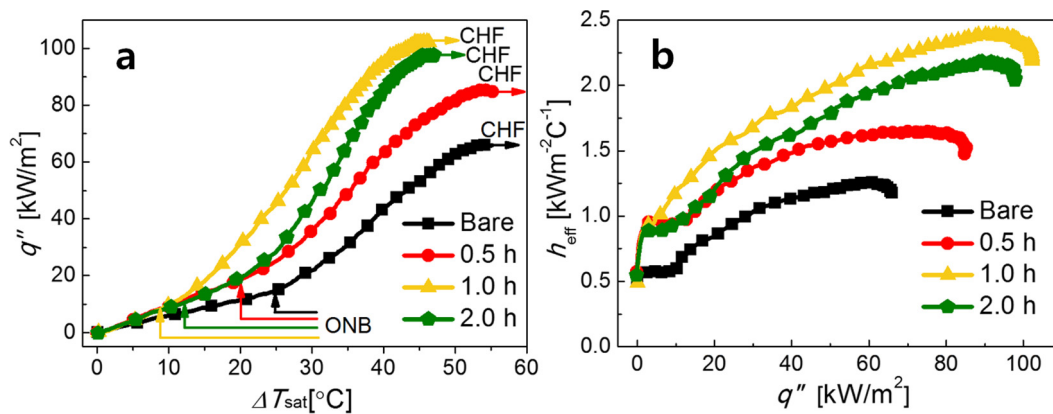


Fig. 6. (a)  $q''$  as a function of  $\Delta T_{sat}$ . (b)  $h_{eff}$  as a function of  $q''$  with  $t_e$  from 0 to 2 h.

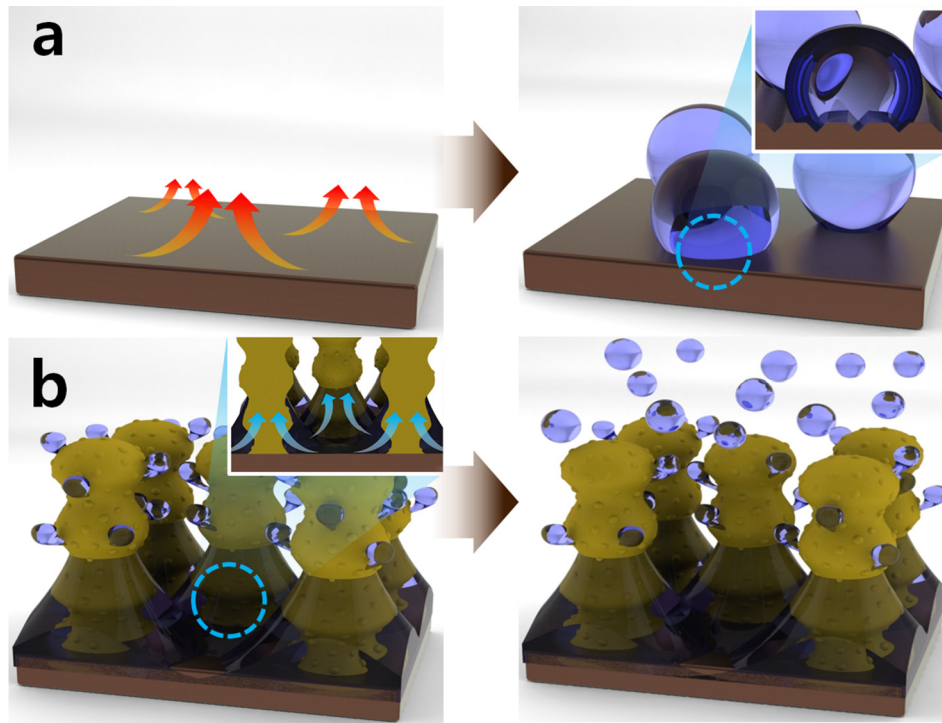


Fig. 7. Schematic of the pool-boiling process.

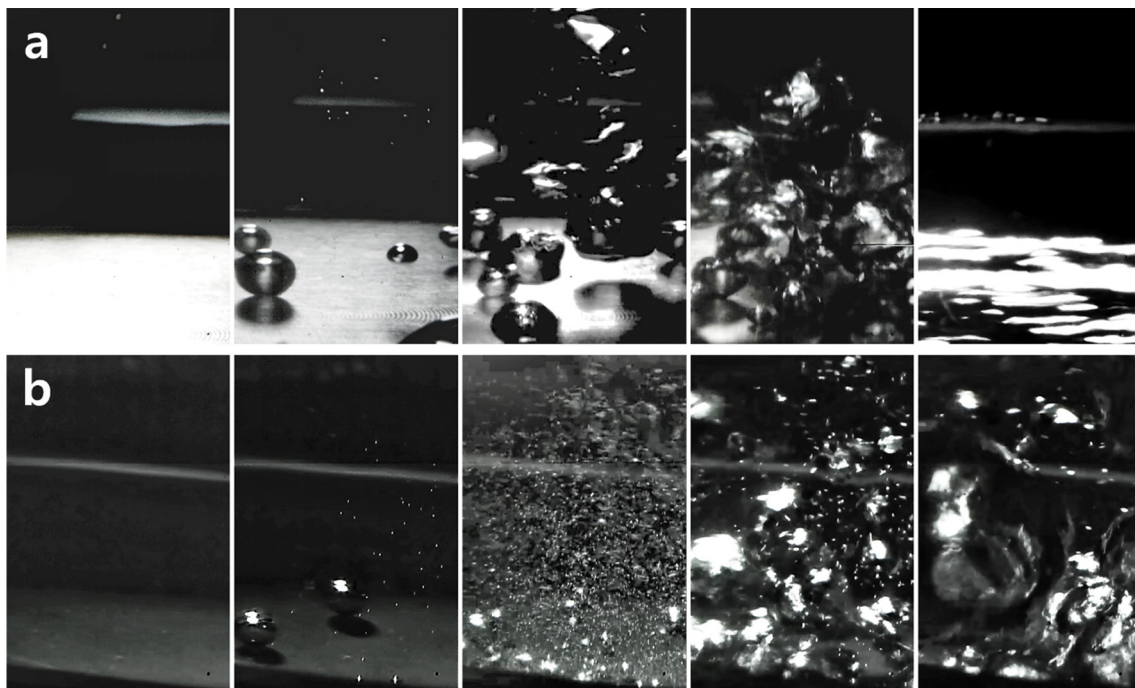


Fig. 8. Photographs of plate pool boiling for natural convection, the ONB, maximum  $h_{\text{eff}}$ , CHF, and transition for an (a) uncoated substrate and when (b)  $t_e = 1$  h.

(Fig. 8b) with nano-pillaring compared to an uncoated substrate (Fig. 8a).

However, CHF does not increase with  $t_e$  as does  $h_{\text{eff}}$ . For  $t_e = 1$  h, CHF is greatest with more heat removed due to the production of more total bubbles. Even though the number of nucleation sites increased with  $t_e$ , CHF does not increase because the bubble path is more tortuous due to the long pillar lengths and the close distances between pillars. For this

morphology, bubbles are attached to the nanotextured surface longer. Clearly, the combination of pillar length and distance between pillars has an effect on  $h_{\text{eff}}$  and CHF and optimal conditions exist. However, in our study, although pillar length can be controlled through  $t_e$ , distances between pillars are random functions of  $\text{BiVO}_4$  particle deposition. To further improve pool boiling, study of the relation of pillar length and separation distance are required.

#### 4. Conclusion

Nano-pillared surfaces built through ESD of BiVO<sub>4</sub> were used to enhance the pool-boiling process. The nano-pillars provided numerous bubble nucleation sites because of increased surface area. As a result, CHF and  $h_{\text{eff}}$  were both enhanced, however, an optimal texturing was identified as excessive texturing hindered the efficient release of nucleated bubbles. An electro-spraying time of 1 h was near optimal under these experimental conditions. The electro-sprayed surfaces were characterized by SEM, AFM, and XPS. The surface wettability, CHF, ONB, and  $h_{\text{eff}}$  were experimentally measured. Snapshots showing bubble nucleation and release were taken and phenomenologically explained.

#### Acknowledgement

This research was supported by the Technology Development Program to Solve Climate Changes of the National Research Foundation of Korea (NRF) funded by the Ministry of Science, ICT & Future Planning (2016M1A2A2936760) and NRF-2017R1A2B4005639. This work was also supported by the National Research Council of Science & Technology (NST) grant by the Korea government (MSIP) (No. CRC-16-02-KICT)

#### References

- Agostini, B., Fabbri, M., Park, J.E., Wojtan, L., Thome, J.R., Michel, B., 2007. State of the art of high heat flux cooling technologies. *Heat Transfer Eng.* 28, 258–281.
- An, S., Kim, D.Y., Lee, J.G., Jo, H.S., Kim, M.W., Al-Deyab, S.S., Choi, J., Yoon, S.S., 2016. Supersonically sprayed reduced graphene oxide film to enhance critical heat flux in pool boiling. *Int. J. Heat Mass Transfer* 98, 124–130.
- Bar-Cohen, A., Arik, M., Ohadi, M., 2006. Direct liquid cooling of high flux micro and nano electronic components. *Proc. IEEE* 94, 1549–1570.
- Choi, J., Jeong, M., 2016. Compact, lightweight, and highly efficient circular heat sink design for high-end PCs. *Appl. Therm. Eng.* 92, 162–171.
- Choi, J., Sung, B., Yoo, J., Kim, C., Borca-Tasciuc, D.-A., 2012. Enhanced miniature loop heat pipe cooling system for high power density electronics. *J. Therm. Sci. Eng. Appl.* 4, 021008.
- Eick, J., Good, R., Neumann, A., 1975. Thermodynamics of contact angles. II. Rough solid surfaces. *J. Colloid Interface Sci.* 53, 235–248.
- Halliday, W., 1991. *Resnick. Fundamentals of Physics.* John Wiley and Sons.
- Holman, J., 2001. *Experimental methods for engineers.*
- Jo, H.S., An, S., Park, H.G., Kim, M.-W., Al-Deyab, S.S., James, S.C., Choi, J., Yoon, S.S., 2017. Enhancement of critical heat flux and superheat through controlled wettability of cuprous-oxide fractal-like nanotextured surfaces in pool boiling. *Int. J. Heat Mass Transfer* 107, 105–111.
- Ju, P., Wang, Y., Sun, Y., Zhang, D., 2016. Controllable one-pot synthesis of a nest-like Bi<sub>2</sub>WO<sub>6</sub>/BiVO<sub>4</sub> composite with enhanced photocatalytic antifouling performance under visible light irradiation. *Dalton Trans.* 45, 4588–4602.
- Kwok, D., Budziak, C., Neumann, A., 1995. Measurements of static and low rate dynamic contact angles by means of an automated capillary rise technique. *J. Colloid Interface Sci.* 173, 143–150.
- Leong, K., Ho, J., Wong, K., 2017. A critical review of pool and flow boiling heat transfer of dielectric fluids on enhanced surfaces. *Appl. Therm. Eng.* 112, 999–1019.
- Marcinichen, J.B., Olivier, J.A., Lamaison, N., Thome, J.R., 2013. Advances in electronics cooling. *Heat Transfer Eng.* 34, 434–446.
- Semenic, T., Lin, Y.Y., Catton, I., Sarraf, D.B., 2008. Use of biporous wicks to remove high heat fluxes. *Appl. Therm. Eng.* 28, 278–283.
- Shabgard, H., Allen, M.J., Sharifi, N., Benn, S.P., Faghri, A., Bergman, T.L., 2015. Heat pipe heat exchangers and heat sinks: opportunities, challenges, applications, analysis, and state of the art. *Int. J. Heat Mass Transfer* 89, 138–158.
- Weibel, J.A., Garimella, S.V., North, M.T., 2010. Characterization of evaporation and boiling from sintered powder wicks fed by capillary action. *Int. J. Heat Mass Transfer* 53, 4204–4215.
- Yoon, H., Mali, M.G., Choi, J.Y., Kim, M.W., Choi, S.K., Park, H., Al-Deyab, S.S., Swihart, M.T., Yarin, A.L., Yoon, S.S., 2015. Nanotextured pillars of electro-sprayed bismuth vanadate for efficient photoelectrochemical water splitting. *Langmuir* 31, 3727–3737.
- Zhang, W., Wang, M., Zhao, W., Wang, B., 2013. Magnetic composite photocatalyst ZnFe<sub>2</sub>O<sub>4</sub>/BiVO<sub>4</sub>: synthesis, characterization, and visible-light photocatalytic activity. *Dalton Trans.* 42, 15464–15474.